Nanoscale

PAPER

View Article Online
View Journal

Cite this: DOI: 10.1039/d5nr05494j

Achieving high energy products in anisotropic Nd–Fe–B/Fe composite thick films by Dy co-sputtering

Chunhao Li,[a,b] Xiaotian Zhao,*[a] Long Liu,*[a] Weibin Cui,[c,d] Qiang Li,[c,d] Zhixing Ye,[e] Bing Li,[a] Wei Liu[a] and Zhidong Zhang[a]

To realize a high magnetization while ensuring a high coercivity in Nd–Fe–B/Fe composite thick films, this work proposes a spatially selective Dy co-sputtering strategy that precisely introduces Dy into surface and interfacial regions. This approach significantly strengthens the magnetocrystalline anisotropy and columnar grain continuity, yielding a coercivity of 1.75 T, a remanence of 1.23 T, and a maximum energy product of 35.2 MGOe. Microstructural analyses reveal that the Dy co-sputtering not only adjusts the local chemical composition to form $(Nd,Dy)_2Fe_{14}B$ with a high magnetocrystalline anisotropy but also induces a microstructural reconstruction, leading to a synergistic enhancement of both coercivity and remanent magnetization. The first-order reversal curve and magnetic domain observations demonstrate that the long-range dipole interaction between the soft- and hard-magnetic layers is enhanced, which shifts the magnetization reversal mechanism from nucleation-dominated to pinning-dominated, evidencing a pronounced magnetic hardening effect. These findings establish that Dy-assisted microstructure optimization and magnetic hardening, together with the high magnetization provided by the Fe soft-magnetic layer, offer an effective pathway for fabricating high-performance Nd–Fe–B/Fe composite thick films being compatible with micro-electromechanical systems.

Received 30th December 2025,
Accepted 11th March 2026

DOI: 10.1039/d5nr05494j

rsc.li/nanoscale

Introduction

Micrometer-scale Nd–Fe–B thick films have broad application prospects in micro-electromechanical systems (MEMSs), micro-actuators, micro-motors, and miniature magnetic sensors due to their high energy density, miniaturization capability, and compatibility with semiconductor processes.[1–3] As high-performance magnetic MEMSs continue to evolve toward integration and miniaturization, magnetic functional layers are required not only to possess high remanence and high coercivity, but also to maintain stable orientation control.[4–6] Therefore, achieving both high magnetization and coercivity in the Nd–Fe–B films of micrometer-thicknesses has become an important research direction in magnetic film technology.[7]

However, as the film thickness increases, the mobility of adsorbed particles and surface diffusion diminish, leading to a sequential transformation in the growth pattern. This evolution produces renucleation, surface roughening, repeated short-column/void structures, and increasingly random out-of-plane crystal orientation, all of which collectively weaken the *c*-axis orientation and magnetic properties.[8] This thickness-induced structural evolution indicates that microstructural stability (particularly a vertical texture) is a key limiting factor for achieving high-performance Nd–Fe–B thick films.[9] In addition to orientation degradation, a prolonged deposition also leads to the gradual accumulation of internal stresses, which accelerates the aggregation and segregation of Nd-rich phases.[10–13] Excessive Nd-rich phases reduce the volume fraction of the $Nd_2Fe_{14}B$ main phase in the film, resulting in a decrease of magnetization. Previous studies have attempted to alleviate deposition stress by introducing Ta spacer-layers. Although they enhance the perpendicular magnetic anisotropy (PMA) and increase the remanent magnetization, the improvement in saturation magnetization was marginal.[14,15]

To suppress the performance degradation of micro thickness Nd–Fe–B films, soft/hard-magnetic composite structures demonstrate potential advantages.[16,17] By precisely controlling the thickness and growth characteristics of each

[a]*Shenyang National Laboratory for Materials Science, Institute of Metal Research, Chinese Academy of Sciences, Shenyang 110016, China. E-mail: xtzhao@imr.ac.cn, lliu16s@imr.ac.cn*
[b]*School of Materials Science and Engineering, University of Science and Technology of China, Shenyang 110016, China*
[c]*Key Laboratory of Electromagnetic Processing of Materials, Northeastern University, Shenyang 110819, China*
[d]*Department of Physics and Chemistry of Materials, School of Materials Science, Northeastern University, Shenyang 110819, China*
[e]*Key Laboratory of Rare Earths, Ganjiang Innovation Academy, Chinese Academy of Sciences, Ganzhou 341119, China*

layer through magnetron sputtering technology, soft /hard-magnetic Nd–Fe–B/Fe multilayer structures can be constructed.[18] In thin-film systems, combining refractory metal spacer-layers (Ta, Mo, *etc*.) enhances saturation magnetization while maintaining sufficient coercivity.[19,20] This approach establishes exchange interactions between the soft magnetic layer and the hard magnetic layer, achieving a maximum energy product of 61 MGOe—representing the highest value for anisotropic nanocomposite thin films.[21,22] Further extending this strategy to soft/hard-magnetic composite thick films, the study reveals that interlayer interactions dominated by long-range dipole interactions play a crucial role in enhancing the magnetic properties.[23–25] However, as the volume fraction of the soft-magnetic layer or the stacked layer count increases, although the saturation can be further enhanced, the coercivity inevitably decreases, which originates from the decoupling between soft- and hard-magnetic layers.[26]

In Nd–Fe–B-based materials, the Dy/Tb element significantly enhances the magnetic crystalline anisotropy of the $Nd_2Fe_{14}B$-based main phase by partially substituting Nd.[27–29] It increases the magnetic reversal energy barrier and suppresses domain wall motion and reverse nucleation, markedly improving coercivity.[30] This magnetic hardening mechanism has been extensively validated in bulk Nd–Fe–B materials.[31] Therefore, numerous studies have also attempted to apply the Dy diffusion method to Nd–Fe–B thin-film systems.[32,33] Ye *et al.* observed a reaction between Dy- and Nd-rich phases in Dy-diffused Nd–Fe–B thick films.[34] However, the thermal diffusion-based Dy introduction method faces several limitations in film systems, such as texture degradation and the difficulty in precisely controlling the diffusion depth.[34] Consequently, although Dy exhibits magnetic hardening effects, achieving simultaneous orientation stability, composition controllability, and magnetic property optimization remains challenging in film processes.

In this study, we propose a spatially selective Dy co-sputtering strategy that fundamentally differs from conventional diffusion approaches. Using this strategy, the magnetic hardening element Dy is introduced into the surface and interfacial regions of the soft/hard-magnetic composite thick film. This approach maintains the high magnetization provided by the long range interaction between the soft-magnetic Fe and Nd–Fe–B layers meanwhile enhancing local magnetic anisotropy to increase coercivity. Furthermore, microstructural analysis indicates that Dy co-sputtering drives columnar grain formation and growth, thereby increasing the effective volume fraction of the $Nd_2Fe_{14}B$ hard phase and further enhancing the magnetization. This ultimately achieves a synergistic enhancement of coercivity and remanent magnetization, significantly improving the maximum energy product. First-order reversal curve (FORC) and magnetic domain imaging analyses further confirm the influence of structural homogeneity on magnetic interactions, as well as the pinning effect in magnetic hardening regions.

Experimental

All thick films were fabricated using a high-vacuum magnetron sputtering system equipped with a co-sputtering module. Before deposition, the chamber pressure was better than 3×10^{-5} Pa, and the Ar pressure was maintained at 0.7 Pa during deposition. The hard-magnetic Nd–Fe–B layer was deposited using an $Nd_{15}Fe_{75}B_{10}$ (atomic percent) alloy target prepared by powder metallurgy, while the soft-magnetic Fe layer, the Ta spacer-layer, and the co-sputtered Dy were deposited using commercial targets with 99.99% purity. The sputtering rates and corresponding DC sputtering powers of each target were calibrated by the weighing method as follows: Nd–Fe–B at 20 Å s^{-1} (300 W), Fe at 3.76 Å s^{-1} (100 W), Ta at 0.78 Å s^{-1} (175 W), and Dy at 0.50 Å s^{-1} (25 W). Ta buffer and capping layers with the same thickness of 50 nm were utilized to enhance the adhesion on the Si substrate and prevent oxidation, respectively. For simplicity, these two Ta layers will not be specified again in the subsequent structural descriptions. As illustrated in Fig. 1(a), to investigate the influence of Dy surface and interfacial co-sputtering on Nd–Fe–B/Fe/Nd–Fe–B composite multilayers, two types of structures were first fabricated on Si substrates: a single Nd–Fe–B layer (4 μm), and a Nd–Fe–B (2 μm)/Ta (10 nm)/Fe (150 nm)/Ta (10 nm)/Nd–Fe–B (2 μm) multilayer structure, referred to as the Nd–Fe–B single layer and the NFN film, respectively. Subsequently, based on the NFN structure, Nd–Fe–B/Dy co-sputtering (hereafter referred to as Dy co-sputtering) was applied at both the soft/hard-magnetic interface and the top and bottom surfaces of the multilayer. By controlling the co-sputtering time, Dy co-sputtered layer thicknesses of 100 nm, 300 nm, and 500 nm were obtained, and the corresponding films were named NFN D100, NFN D300, and NFN D500. During the film deposition process, the Nd–Fe–B target remains continuously activated. When deposition reaches the preset layer, the Dy target is activated for sputtering, thereby achieving simultaneous deposition of the Nd–Fe–B target and the Dy target. Under these process conditions, the thickness of the independently deposited Nd–Fe–B layer is consistently maintained at 2 μm. The "Nd–Fe–B/Dy co-sputtered thickness" is defined as the corresponding Nd–Fe–B deposition thickness achieved when the Dy target is activated (the deposition thickness of Dy is disregarded in this context). Based on the sputtering time and the Dy sputtering rate, the effective Dy thickness deposited during co-sputtering was calculated to be approximately 10 nm, 30 nm, and 50 nm, respectively. To suppress interfacial inter-diffusion, a 10 nm Ta spacer-layer was inserted between the Nd–Fe–B and Fe layers. The Nd–Fe–B layers, Ta spacer-layer, and Fe layer were all deposited at 500 °C. Finally, all films were annealed *in situ* at 780 °C under an Ar atmosphere of 0.7 Pa for 20 minutes. Following annealing, the films were cooled to room temperature with the chamber temperature under the same atmosphere conditions.

A Bruker D8 Advance X-ray diffractometer (XRD) was used to analyze the crystalline phases of the films. Magnetic hysteresis loops and FORCs were measured using a superconducting quantum interference device magnetometer (SQUID). The

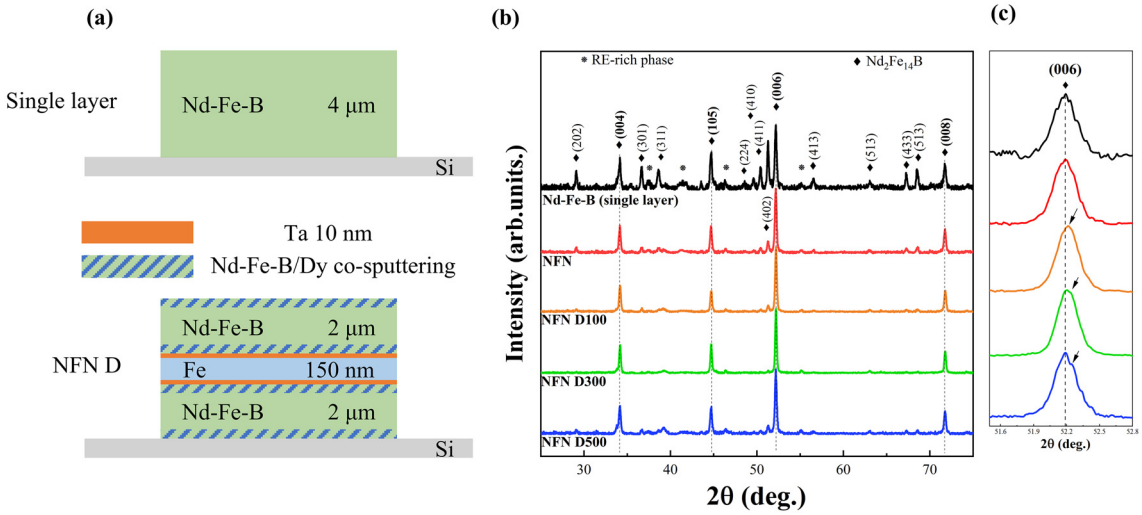

Fig. 1 (a) Schematic diagrams of the Nd–Fe–B single layer film and the Nd–Fe–B/Ta/Fe/Ta/Nd–Fe–B (NFN) composite thick film structure with Dy co-sputtering on the surface and interface. (b) XRD patterns of the Nd–Fe–B single layer film, NFN, NFN D100, NFN D300, and NFN D500 films. (c) Enlarged XRD view of the (006) peak of the $Nd_2Fe_{14}B$ phase.

microstructure and morphology were examined using a ZEISS SUPRA 55 SAPPHIRE field-emission scanning electron microscope (FESEM) and a Talos F200X G2 high-resolution transmission electron microscope (HRTEM). To further determine the elemental distribution, quantitative area scanning was performed using a SHIMADZU EPMA-1600 electron probe microanalyzer (EPMA). At room temperature, magnetic domain structures were characterized *in situ* using a physical property measurement system (PPMS) equipped with a scanning probe microscopy (SPM) module over a scanning area of 6 μm × 6 μm. The surface morphology was obtained in tapping mode, followed by lifting the probe tip 100 nm above the surface to acquire magnetic domain images.

Results and discussion

Structure and magnetic properties of Nd–Fe–B/Fe thick films with Dy co-sputtering

Fig. 1(b) shows the XRD patterns of the Nd–Fe–B single layer film and NFN, NFN D100, NFN D300, and NFN D500 films. The Nd–Fe–B single layer film exhibits a certain degree of the *c*-axis texture, as evidenced by the coexistence of *c*-axis related diffraction peaks such as (006) and (008) together with non-*c*-axis diffraction peaks including (402). In contrast, the NFN film shows dominant (006), (004), and (008) diffraction peaks, indicating a pronounced out-of-plane orientation, which is attributed to the introduction of the Ta spacer-layer.[14,35] After the introduction of Dy co-sputtering, the main diffraction peaks of NFN D100, NFN D300, and NFN D500 films remain consistent with those of the NFN film, indicating that it does not significantly alter the overall texture. However, in the enlarged view in Fig. 1(c), the (006) peak gradually shifts toward higher angles with increasing Dy co-sputtering thickness. The smaller ionic radius of Dy^{3+} compared with that of Nd^{3+} indicates a certain lattice contraction, demonstrating that Dy enters the $Nd_2Fe_{14}B$ lattice and partially substitutes for Nd. This confirms that Nd–Fe–B/Dy co-sputtering achieves an effective Dy incorporation, which potentially enhances the magnetocrystalline anisotropy. Additionally, the zero-field cooling M–T curves for the Nd–Fe–B single layer and the NFN D300 films shown in Fig. S1 reveal that the NFN D300 film exhibits a higher spin reorientation temperature.

Fig. 2(a) and (b) show the out-of-plane and in-plane hysteresis loops for the Nd–Fe–B single layer film and the composite thick films with different Dy co-sputtering thicknesses, respectively. The films with Dy co-sputtering exhibit a more obvious distinction between in-plane and out-of-plane hysteresis loops compared to the NFN film and Nd–Fe–B single layer films, demonstrating stronger PMA. Fig. 2(c) and (d) present magnetic property comparison diagrams obtained from out-of-plane hysteresis loops. The dashed lines represent the magnetic properties of the Nd–Fe–B single layer film. In contrast to the single layer film, the NFN film exhibits decreased coercivity but significantly increased remanent polarization (J_r) and saturation polarization (J_s), leading to an increased maximum energy product ($(BH)_{max}$) from 13.6 MGOe to 22.0 MGOe (a 62% increase). In previous work, the $(BH)_{max}$ value of a soft/hard composite trilayer film was improved by only 28%, ultimately reaching 22.5 MGOe through multilayer stacking.[23,26] This demonstrates the effectiveness of the structural design adjustments in this work. For films with Dy co-sputtering, the coercivity of NFN D100, NFN D300, and NFN D500 films increases initially and then decreases with increasing Dy co-sputtering thickness. The NFN D300 film reaches a maximum of 1.75 T, better than that of the Nd–Fe–B single layer film. On the other hand, the polarization and remanence ratio unexpectedly exhibit the same trend, while the remanence and the

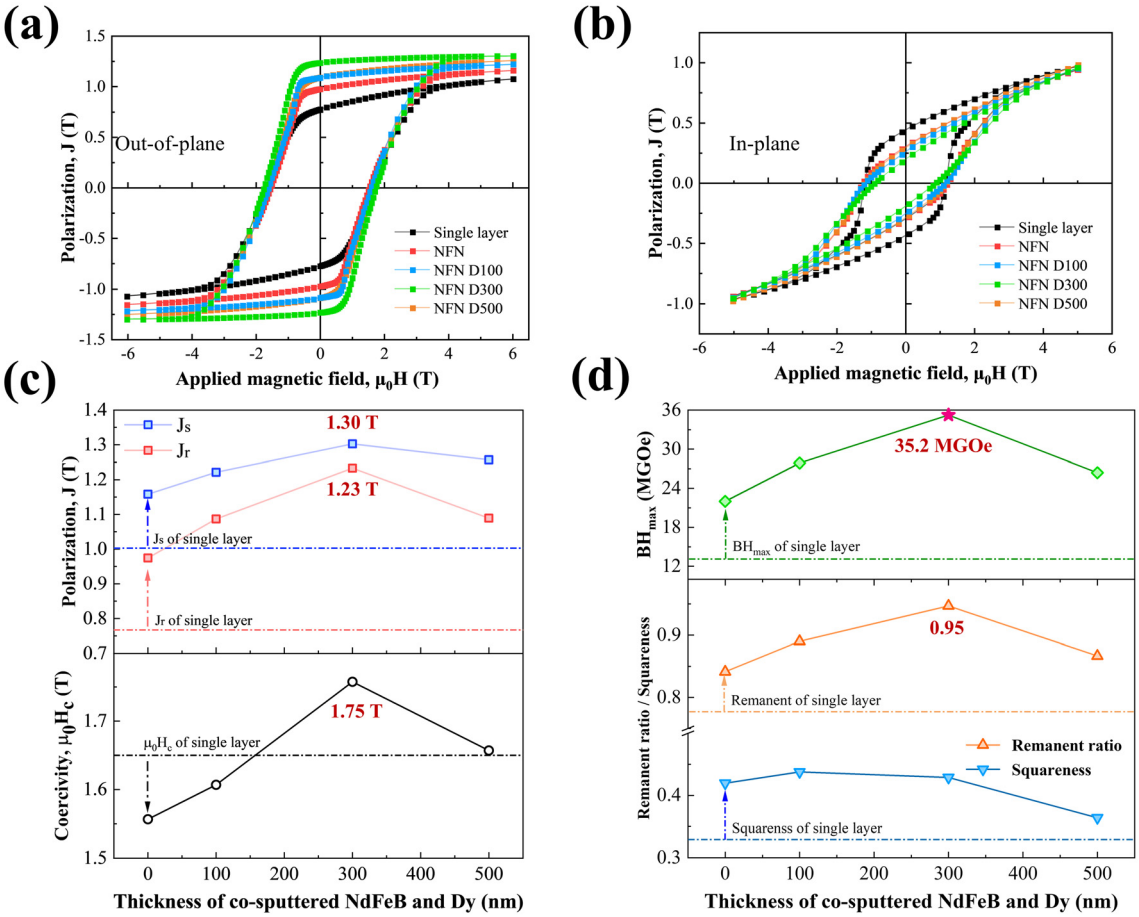

Fig. 2 Room-temperature (a) out-of-plane and (b) in-plane magnetic hysteresis loops of the Nd–Fe–B single layer film and NFN, NFN D100, NFN D300, and NFN D500 films. (c) Comparison of coercivity, saturation magnetization, and remanence extracted from (a). (d) Comparison of the remanent ratio, squareness, and $(BH)_{max}$ calculated from (a).

remanence ratio reach 1.23 T and 0.95, respectively. Ultimately, a maximum energy product of 35.2 MGOe is obtained for the NFN D300 film, a further 60% increase compared to that for the NFN film. This high $(BH)_{max}$ value is attributed to the cooperation of the Fe layer and Dy. The soft-magnetic Fe layer, with appropriate thickness and high J_s, establishes effective long-range interlayer interactions with the Nd–Fe–B hard-magnetic layers, thereby significantly enhancing the polarization. In Dy-doped Nd–Fe–B, $Dy_2Fe_{14}B$ possesses a strong uniaxial magnetocrystalline anisotropy, enhancing anisotropy along the *c*-axis and increasing coercivity. However, excess Dy results in intensified antiferromagnetic coupling with Fe, reducing polarization.[34,36] Therefore, appropriate Dy co-sputtering on the surface and at interfaces in Nd–Fe–B/Fe composite multilayer films is beneficial for enhancing the PMA and polarization, achieving a high $(BH)_{max}$ value.

Microstructures of Nd–Fe–B/Fe thick films with Dy co-sputtering

Evolution of the magnetic properties is further investigated by cross-sectional morphology observations and elemental distribution analysis. Fig. 3(a) and (b) illustrate the cross-sectional SEM images of the Nd–Fe–B single layer film and the NFN film. The backscattered electron (BSE) images, and Nd, Fe and Ta elemental distributions of the Nd–Fe–B single layer film are shown in Fig. 3(a1). The Nd–Fe–B single layer film shows a columnar texture near the capping layer and a small strip-like texture near the buffer layer. EPMA elemental mapping reveals a significantly higher Nd concentration near the Ta buffer layer. This distribution originates from stress-induced compositional segregation during downward film growth, which drives Nd migration toward the buffer layer and leads to the formation of Nd-rich phases.[37] Therefore, the strip-like texture regions present more Nd rich phases, while the columnar texture regions exhibit uniform distribution of Nd and Fe elements. For the NFN film, similar textures are observed between the spacer-layer and the capping layer, while more obvious stripe-like textures are evident near the buffer layer. Fig. S2 presents the EPMA elemental map of the NFN film. It reveals that Nd-rich regions similar to those of the Nd–Fe–B single layer film still exist above the Ta spacer-layer, while the Fe distribution remains non-uniform. This indicates that the multilayer structure design did not effectively mitigate stress-induced Nd accumulation. Cross-sectional SEM images of NFN

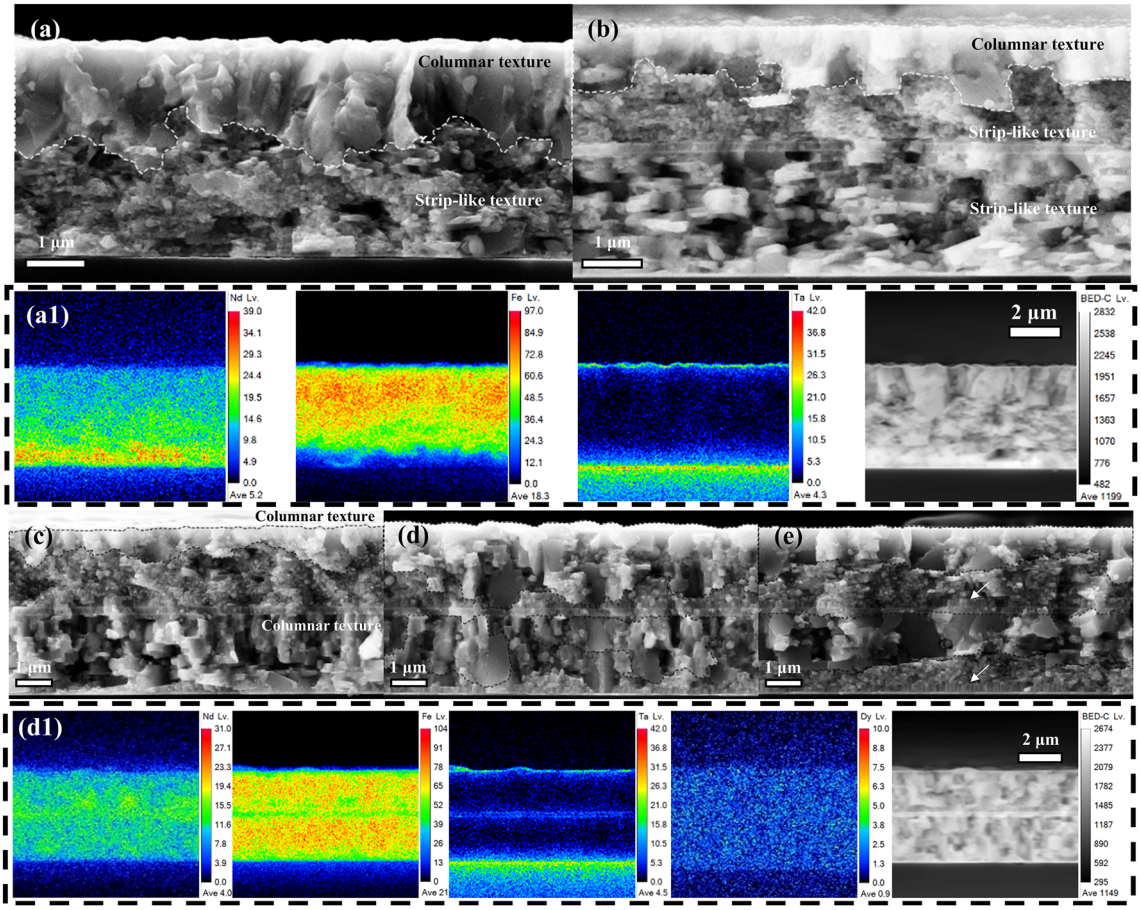

Fig. 3 (a) Cross-sectional SEM image of the Nd–Fe–B single layer film. (a1) Cross-sectional BSE-SEM image of the Nd–Fe–B single layer film, along with elemental content mapping of Nd, Fe, and Ta. (b) Cross-sectional SEM image of the NFN film. (c–e) Cross-sectional SEM images of the NFN D100, NFN D300, and NFN D500 films, respectively. (d1) Cross-sectional BSE-SEM image of the NFN D300 film, along with the elemental distribution maps of Nd, Fe, Ta and Dy.

D100, NFN D300 and NFN D500 films with the Dy co-sputtered surface and interface regions are illustrated in Fig. 3(c)–(e). For the NFN D100 film, the overall texture remains similar to that of the undoped NFN film, but the strip-like textures between the spacer and buffer layer begin to transform into a columnar texture. This trend becomes more significant in the NFN D300 film, where extensive columnar textures appear between the capping layer and the spacer-layer. The corresponding elemental distribution (Fig. 3(d1)) reveals that Dy diffuses through the entire film thickness, and Nd segregation is no longer observed. Combined with the distribution of Ta elements, it is confirmed that the spacer-layer effectively suppresses further downward the diffusion of Nd, allowing the $Nd_2Fe_{14}B$ phase below the spacer-layer to nucleate and grow normally, thereby forming the columnar textures. When the Dy co-sputtering thickness is further increased to 500 nm, the columnar texture still dominates, and a significant increase in strip-like texture regions is observed. This structural evolution is related to the excessive Dy incorporation: excess Dy tends to form intergranular phases at grain boundaries, reducing the volume fraction of the hard-magnetic phase, ultimately deteriorating the magnetic properties. Consequently, an appropriate amount of Dy co-sputtering (~300 nm) at the interface and surface regions of the Nd–Fe–B/Fe composite thick film improves texture uniformity, resulting in a better *c*-axis orientation.

Fine analysis of the microstructure is crucial for understanding the evolution mechanism of the magnetic properties. Fig. 4(a) presents the cross-sectional TEM image of the NFN film, where the Ta buffer and capping layers are on the left and right parts. The Ta spacer-layer and the intermediate soft-magnetic Fe layer are clearly identified. The Ta layers achieve effective isolation, and the grain morphology on both sides exhibits significant differences. Fig. 4(b) provides an enlarged view of region B, where a grain has a size of approximately 297 nm × 494 nm, which demonstrates the normal nucleation and growth of hard-magnetic grains in this region. Above the Ta spacer-layer, a ~1.5 μm region of stacked smaller strip-like grains is observed, with a representative grain size of 52 nm × 103 nm in region C (Fig. 4(c)). The columnar grains grow from the capping layer, with a size of approximately 505 nm × 364 nm (Fig. 4(d)). The HRTEM image in Fig. 4(e) and its fast Fourier transform (FFT) analysis confirm that the columnar

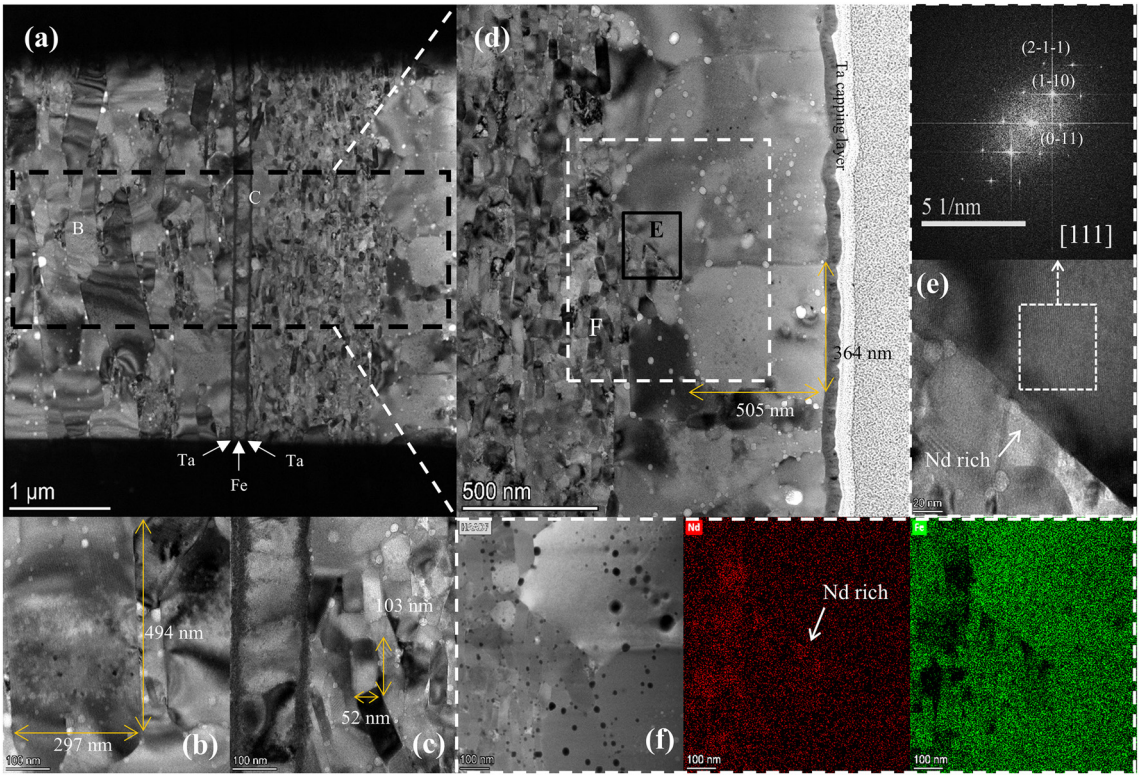

Fig. 4 (a) Cross-sectional TEM image of the NFN film. Enlarged views of regions B (b) and C (c), respectively, within the black dashed box in (a). (d) Enlarged view near the Ta capping layer. (e) HRTEM image of region E in (d) and FFT results. (f) HADDF image of region F in (d), along with the elemental distribution maps of Nd and Fe in the corresponding area.

grain corresponds to the $Nd_2Fe_{14}B$ phase with a [111] zone axis. HAADF imaging and elemental mapping of region F (Fig. 4(f)) reveal pronounced Nd enrichment at the grain boundaries between strip-like and columnar grains, while no pronounced Nd segregation is observed between columnar grains. Therefore, it is inferred that the Nd segregation suppresses further grain growth, limiting the effective volume fraction of the $Nd_2Fe_{14}B$ hard-magnetic phase, resulting in a magnetization lower than that expected.[38] In a word, the isolating effect of the Ta interlayer in NFN films not only establishes an effective long-range interaction between soft- and hard-magnetic layers but also hinders Nd migration toward the buffer layer, partially optimizing the formation of the $Nd_2Fe_{14}B$ main phase.

Fig. 5 demonstrates the cross-sectional TEM results of the NFN D300 film. Compared with the NFN film, Dy doping induces a significant structural evolution while maintaining a distinct Ta/Fe/Ta layered interface. Four typical regions have been selected from the buffer layer to the capping layer for enlarged observation (black boxes in Fig. 5(a), enlarged in Fig. 5(b)–(e)). In the buffer layer shown in Fig. 5(b), in addition to fine strip-like grains similar to those in the NFN film, small columnar grains unexpectedly appear within the Dy co-sputtering thickness of ~300 nm, which grow upward from the buffer layer. A typical columnar grain in this region has a size of approximately 795 nm × 249 nm (Fig. 5(c)). Grain intersection leads to Nd enrichment, suppressing grain growth and producing fine strip-like grains, further substantiating the preceding analysis. In Fig. 5(d), the small columnar grains also appear near the Ta spacer-layer (the same columnar texture is also seen in Fig. 3(c) at the corresponding position of the cross-sectional SEM image for NFN D500, indicated by white arrows). Similarly constrained by the bidirectional grain growth, the fine strip-like grain region shrinks to ~400 nm. The columnar grains in region F, characterized by FFT, belong to the $Nd_2Fe_{14}B$ phase with a [210] zone axis (Fig. 5(f)). Fig. 5(g) shows the HAADF-EDS elemental map of region G, where grain boundaries in the strip-like grain areas are primarily composed of Nd, with minor amounts of Dy and Ta. However, Dy is predominantly distributed inside the grains, confirming that Dy is successfully dissolved into the $Nd_2Fe_{14}B$ lattice, consistent with the XRD and EPMA results. Additionally, the columnar grains near the capping layer further increase in size to ~795 nm × 366 nm, and the columnar grain region expands to more than 1 μm. In summary, Nd–Fe–B/Dy co-sputtering at the surface and interface regions induces the following microstructural reconstruction: (1) promotes the transition of strip-like grains between the buffer layer and Ta spacer-layer into larger columnar grains; (2) enlarges the grain size and distribution range of columnar grains between the Ta spacer-layer and the capping layer and (3) induces the formation of additional $(Nd,Dy)_2Fe_{14}B$ columnar grains in the co-sputtering regions.

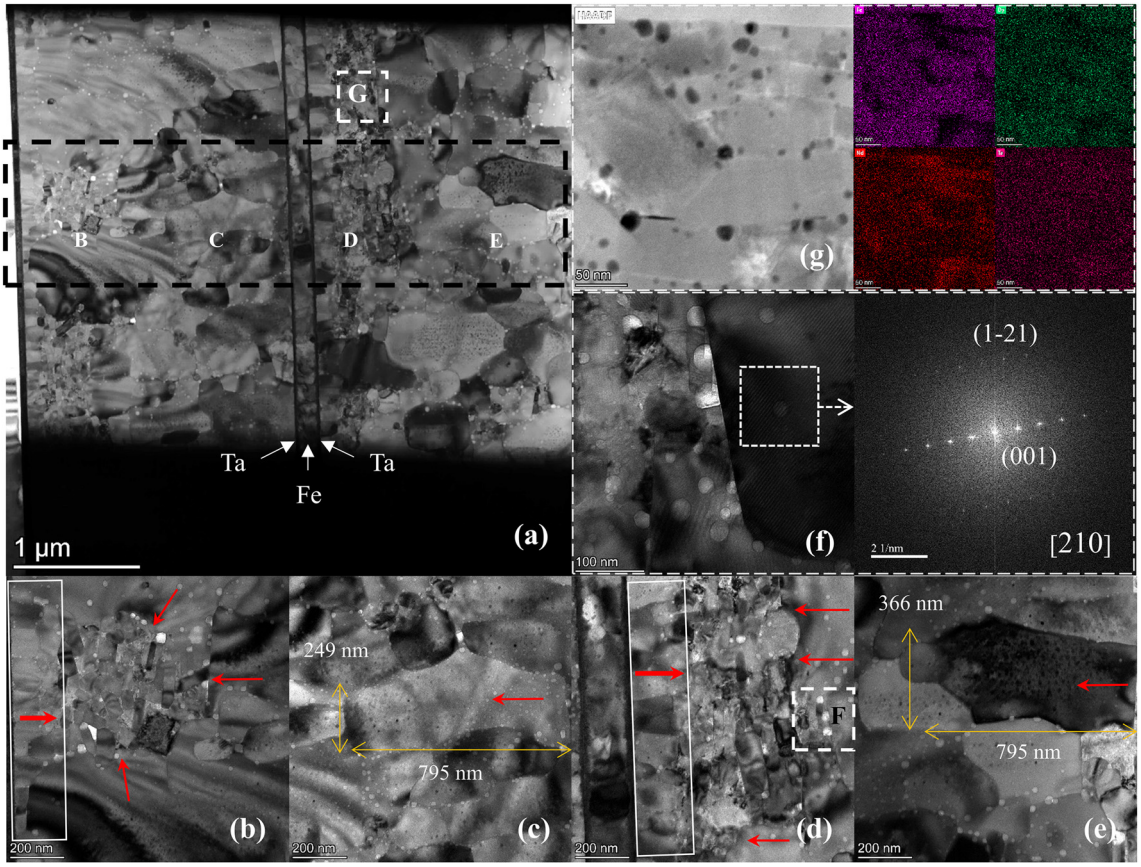

Fig. 5 (a) Cross-sectional TEM image of the NFN D300 film. (b–e) Enlarged views of regions B, C, D, and E, respectively, within the black dashed box in (a). The red arrows indicate the direction of growth. (f) Enlarged view of region F in (d) and its FFT results. (g) HADDF image of region G in (a), along with elemental distribution maps for Nd, Fe, Dy, and Ta in the corresponding area.

These results clearly demonstrate that Dy co-sputtering and Dy diffusion effectively facilitate the growth of $Nd_2Fe_{14}B$ grains, which directly contributes to the significant increase in magnetization. This conclusion is consistent with the thermodynamic calculations, indicating that partial substitution of Nd with Dy suppresses the formation of γ-Fe and Nd_2Fe_{17} phases and instead stabilizes the $Nd_2Fe_{14}B$ hard-magnetic phase.[39–41] More importantly, Dy co-sputtering significantly enhances the structural uniformity and continuity of the hard-magnetic layer. The effect of Dy doping essentially depends on the competition between reducing nucleation energy and forming intergranular phases. Appropriate Dy co-sputtering not only improves coercivity by enhancing magnetocrystalline anisotropy through localized chemical composition adjustment, but also further induces the *c*-axis orientation of the hard-magnetic layer and promotes growth of the main phase, increasing the main phase volume fraction and thereby enhancing magnetization.

Magnetic interactions of Nd–Fe–B/Fe thick films with Dy co sputtering

The structure of the hard-magnetic layer significantly influences the coupling strength and magnetization reversal behavior of soft/hard composite thick films. To reveal the influence of Dy-induced microstructural reconstruction on magnetic interactions, the FORC method was employed. During the FORC measurement, the film was first saturated, and then the magnetic field $\mu_0 H$ was gradually increased from different reversal fields $\mu_0 H_r$, while recording the magnetization M up to the saturation field. Fig. 7(a), (d) and (g) represent the normalized out-of-plane FORC results for the Nd–Fe–B single layer film, the NFN film, and the NFN D300 film, respectively. The FORC distribution is obtained using eqn (1), and the coercive field $\mu_0 H_c$ and the interaction field $\mu_0 H_u$ are derived through the coordinate transformations given in eqn (2) and (3).[42–45]

$$\rho(H, H_r) = -\partial^2 M(H, H_r)/2\partial H \partial H_r \quad (1)$$

$$\mu_0 H_c = (\mu_0 H - \mu_0 H_r)/2 \quad (2)$$

$$\mu_0 H_u = (\mu_0 H + \mu_0 H_r)/2 \quad (3)$$

Fig. 6(b) shows the FORC distribution of the Nd–Fe–B single layer film in the $\mu_0 H_r - \mu_0 H$ coordinate, exhibiting a typical "wishbone" pattern. Before −0.34 T (point 1), the ρ values remain close to zero, indicating that the magnetization process is essentially reversible. In the range from −0.34 T to −3.73 T (point 3), the ρ values increase sharply, forming a con-

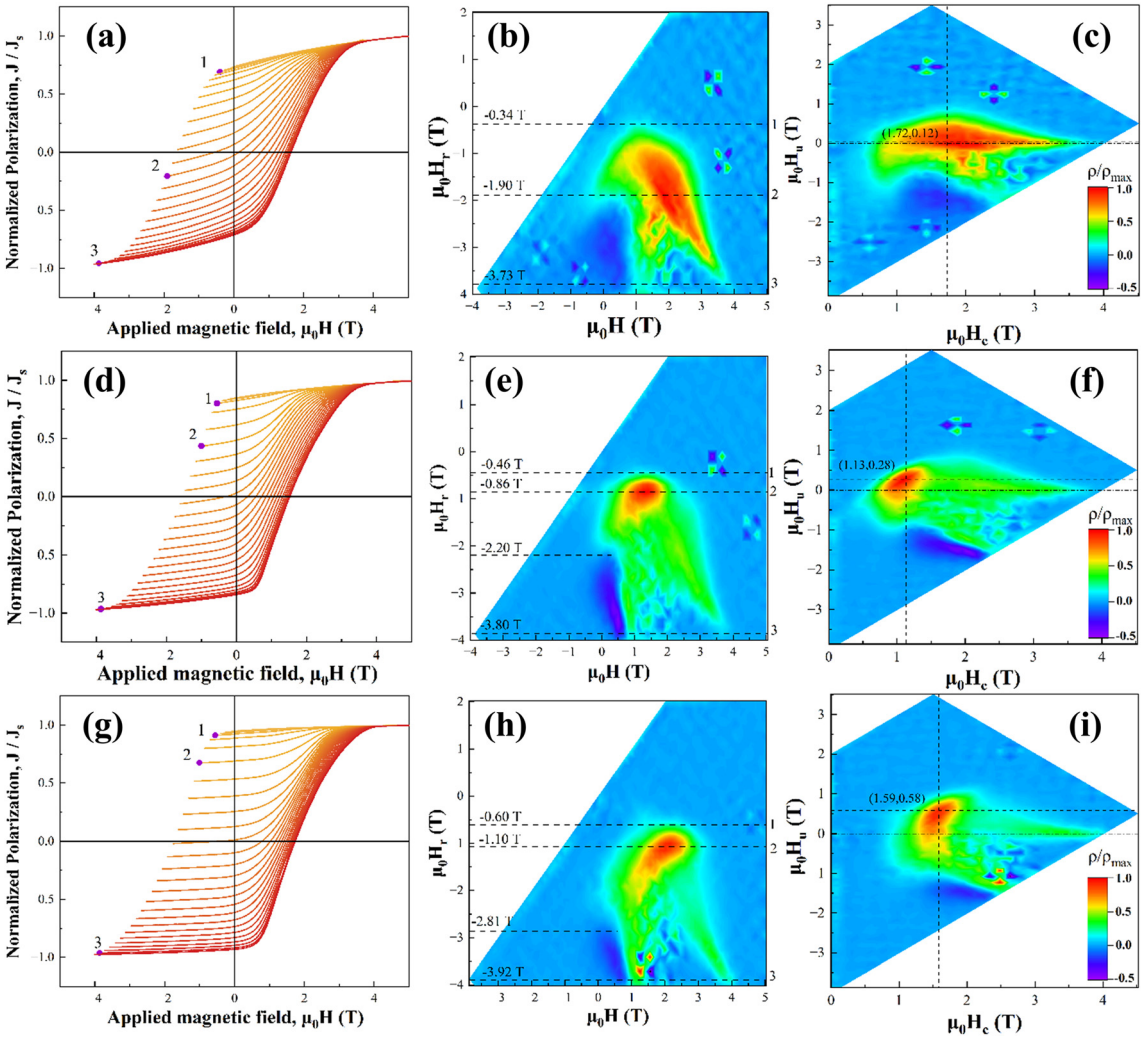

Fig. 6 (a, d, and g) Normalized out-of-plane FORCs for the Nd–Fe–B single layer film, the NFN film, and the NFN D300 film, respectively. (b, e and h) FORC distribution in the $\mu_0H_r - \mu_0H$ coordinates calculated based on the FORCs. (c, f and i) FORC distribution in the $\mu_0H_c - \mu_0H_u$ coordinates obtained after coordinate transformation.

tinuous red high-intensity region, and reach a peak at −1.90 T (point 2), demonstrating that a strong irreversible magnetization reversal is triggered under different μ_0H_r values. The purple negative region appears after the reversal peak marks the onset of the negative saturation state. Fig. 6(c) presents the FORC distribution converted to the $\mu_0H_c - \mu_0H_u$ coordinate. The red high-intensity region is mainly distributed along the μ_0H_c axis, indicating the presence of multiple coercivity components, which is consistent with the poor *c*-axis texture and the presence of the Nd-rich phase. The ρ_{max} is located at (1.72 T, 0.12 T), lying on the positive side of the μ_0H_u axis, suggesting the weak dipolar interaction according to the Pike model.[42,44]

Fig. 6(e) and (h) illustrate the FORC distributions for the NFN and NFN D300 films, and their corresponding $\mu_0H_c - \mu_0H_u$ converted distributions are shown in Fig. 7(f) and (i). The onset of irreversible reversal for NFN and NFN D300 films occurs at −0.46 T and −0.60 T, respectively, reaching maximum values at −0.86 T and −1.10 T, and finally ending at −3.80 T and −3.92 T. Compared with the Nd–Fe–B single layer film, the NFN film still exhibits a "wishbone" structure, but the red high-intensity region becomes more concentrated. For the NFN D300 film, this region further converges, and the green trailing region is significantly reduced, indicating a more cooperative and uniform magnetization reversal. In addition, the starting fields for negative saturation appear at −2.20 T and −2.81 T for the NFN and NFN D300 films, respectively, confirming the higher magnetization of the latter. In the $\mu_0H_c - \mu_0H_u$ coordinate, the coercivity distribution of the NFN film remains broad, and a portion of high-coercivity components (green region) is still observed. The ρ_{max} is located at (1.13 T, 0.28 T) and is significantly shifted toward the positive μ_0H_u axis compared with the single layer film, indicating an enhanced interlayer dipolar interaction. This originates from the long-range coupling between the soft-magnetic Fe layer and the hard-magnetic Nd–Fe–B layers, which contributes to

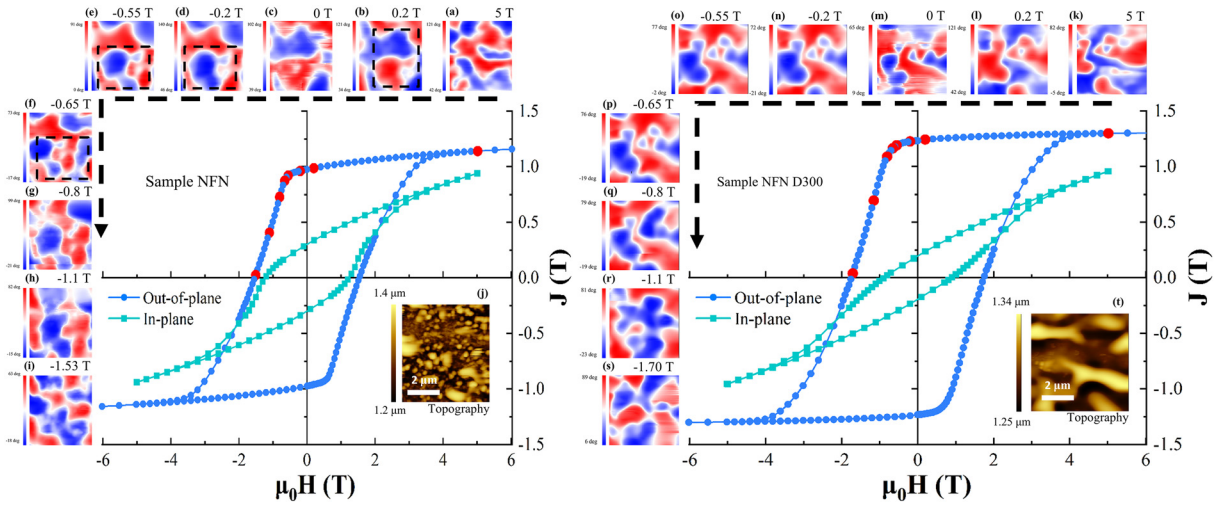

Fig. 7 Out-of-plane and in-plane hysteresis loops for NFN and NFN D300 films, and the corresponding magnetic domain patterns during the out-of-plane demagnetization process for the NFN film (a–i) and the NFN D300 film (k–s), respectively. (j) and (t) Surface topography of the NFN and NFN D300 films, respectively.

the improvement of the magnetization. After introducing Dy co-sputtering, the FORC distribution of the NFN D300 film transitions from being distributed along the $\mu_0 H_c$ axis to being aligned along the $\mu_0 H_u$ axis, with the coercivity distribution becoming more concentrated. The ρ_{max} further shifts to (1.59 T, 0.58 T), indicating stronger interlayer dipolar interaction. In a word, FORC analyses confirm that the microstructural reconstruction induced by Nd–Fe–B/Dy co-sputtering effectively enhances the long-range dipole interactions between the soft- and the hard-magnetic layers, which promotes a more cooperative magnetization reversal process, and ultimately improves magnetic performance.

Coercivity mechanism of Nd–Fe–B/Fe thick films with Dy co-sputtering

To intuitively observe the microscopic origin of the enhanced dipolar interaction between the soft- and hard-magnetic layers, the evolution of surface magnetic domains during the demagnetization process was examined for NFN and NFN D300 films in Fig. 7. The evolution of surface magnetic domains can effectively reflect the influence of microstructural reconstruction on the soft/hard magnetic interaction. First, it can be observed in Fig. 7(j) and (t) that the surface topography of the Nd–Fe–B single layer film exhibits a significant difference from that of the NFN D300 film. To systematically analyze the effect of Dy co-sputtering on the surface roughness of the thick films, SEM characterization results of all films are presented in the SI (Fig. S3). The results reveal that Dy co-sputtering effectively improves surface roughness. As shown in Fig. 7(a), (b) and (d)–(f), the NFN film exhibits pronounced changes in the domain morphology when the magnetic field decreases from +5 T to +0.2 T, indicating the existence of abundant reverse-domain nucleation sites. The magnetization state continuously changes with the applied field. Even within +0.2 T to 0 T and −0.2 T to −0.65 T, local variations in the magnetic domain structure caused by domain wall motion (black dashed rectangles) are clearly observed, revealing that the coercivity mechanism is dominated by the nucleation mechanism. This nucleation-dominated reversal generates numerous early-formed reverse domains, leading to locally premature magnetization reversal and an incoherent reversal process. When the field decreases below −0.65 T, the magnetization drops sharply due to a rapid expansion of reverse domains, accompanied by significant changes in the domain morphology. In contrast, the NFN D300 film exhibits a fundamentally different domain behavior (Fig. 7(k)–(p)). As the field decreases from positive saturation to −0.8 T, the overall domain structure remains stable, with only minor local changes, indicating a highly cooperative magnetization reversal process. A drastic drop in magnetization and a significant change in the domain morphology occur only when the field becomes lower than −0.8 T. This behavior suggests that the coercivity mechanism of the NFN D300 film is dominated by the pinning mechanism, originating from the strong magnetocrystalline anisotropy of the $(Nd,Dy)_2Fe_{14}B$ phase. Consequently, the columnar grains induced in the Dy co-sputtering regions, together with the Nd- and Dy-enriched grain boundaries (as shown in Fig. 5), act as strong pinning centers that effectively impede the motion of magnetic domain walls. This magnetization hardening effect prevents premature reversal in regions that are more susceptible to interference from stray magnetic fields, such as thin film surfaces or grain boundary phase regions. As a result, Nd–Fe–B/Fe composite thick films with Dy co-sputtering maintain uniform magnetization across a wide magnetic field range.

Conclusions

This work systematically elucidates the critical role of spatially selective Dy co-sputtering in governing the structural and mag-

netic evolution of Nd–Fe–B/Fe composite thick films. Appropriate Dy incorporation significantly enhances the magnetocrystalline anisotropy while preserving texture quality, resulting in a coercivity of 1.75 T, a remanence of 1.23 T, a remanence ratio of 0.95, and a maximum energy product of 35.2 MGOe. Microstructural analyses reveal that Dy co-sputtering drives the growth and extension of $Nd_2Fe_{14}B$ columnar grains and induces the formation of high magnetocrystalline anisotropic $(Nd,Dy)_2Fe_{14}B$ columnar grains within regions originally dominated by Nd-rich phases. These structural modifications increase the effective fraction of the hard-magnetic phase, improve columnar grain continuity, and consequently enhance overall magnetization. FORC and magnetic domain observations demonstrate that the Dy-induced microstructural reconstruction strengthens long-range dipolar interactions between the soft- and hard-magnetic layers and introduces a pronounced magnetic hardening effect. This transforms the magnetization reversal mechanism from nucleation-dominated to pinning-dominated behavior. In summary, the combination of Dy-induced microstructure optimization and magnetic hardening with the high magnetization contribution of the Fe soft-magnetic layer achieves a high energy product in the composite thick films. This strategy effectively overcomes the conventional trade-off between magnetization and coercivity, offering a robust and MEMS-compatible route for fabricating high-performance Nd–Fe–B/Fe composite thick films.

Author contributions

Chunhao Li: conceptualization, data curation, formal analysis, investigation, methodology, validation, and writing – original draft. Xiaotian Zhao: conceptualization, methodology, and resources. Long Liu: methodology and formal analysis. Weibin Cui: writing – review & editing and resources. Qiang Li: data curation and software. Zhixing Ye: software and validation. Bing Li: resources. Wei Liu: methodology, writing – review & editing, and funding acquisition. Zhidong Zhang: writing – review & editing.

Conflicts of interest

There are no conflicts to declare.

Data availability

Data will be made available on request.

Supplementary information (SI) is available. See DOI: https://doi.org/10.1039/d5nr05494j.

Acknowledgements

This work has been supported by the National Key R&D Program of China (2023YFB3507301 and 2021YFB3500303) and the National Natural Science Foundation of China under projects 52571236 and 52501263.

References

1 I. Lecerf, J. E. Angulo-Cervera, F. Orlandini-Keller, P. Moritz, F. Mathieu, D. Bourrier, S. Charlot, L. Nicu, T. Leïchlé, T. Devillers, R. Haettel, N. M. Dempsey, T. Blon and L. Lacroix, *Adv. Mater. Technol.*, 2025, **10**, 2401817.
2 J. Liu, X. Hou, J. Liu, X. Bi, H. Wu, J. Zhang, L. Niu, W. Chen, J. He and X. Chou, *Adv. Mater. Technol.*, 2024, **9**, 2302076.
3 Y. Jiang, T. Fujita, M. Uehara, D. Zhang, J. Cai, K. Higuchi and K. Maenaka, *Appl. Phys. Express*, 2011, **4**, 116401.
4 H. Hu, C. Zhang, X. Lai, H. Dai, C. Pan, H. Sun, D. Tang, Z. Hu, J. Fu, T. Li and P. Zhao, *npj Flex. Electron.*, 2024, **8**, 42.
5 F. Dumas-Bouchiat, L. F. Zanini, M. Kustov, N. M. Dempsey, R. Grechishkin, K. Hasselbach, J. C. Orlianges, C. Champeaux, A. Catherinot and D. Givord, *Appl. Phys. Lett.*, 2010, **96**, 102511.
6 K. Nagai, N. Sugita and T. Shinshi, *Micromachines*, 2024, **15**, 248.
7 . D. P. Arnold and W. Naigang, *J. Microelectromech. Syst.*, 2009, **18**, 1255–1266.
8 Q. Yao, W. Liu, W. B. Cui, F. Yang, X. G. Zhao and Z. D. Zhang, *J. Mater. Res.*, 2009, **24**, 2802–2812.
9 Z. X. Ye, X. T. Zhao, W. Liu, L. Liu, J. X. Wu, Y. Li, J. Ma, H. Z. Ju, Y. H. Song and Z. D. Zhang, *J. Alloys Compd.*, 2022, **923**, 166477.
10 T. Shima, A. Kamegawa, K. Hono and H. Fujimori, *Appl. Phys. Lett.*, 2001, **78**, 2049–2051.
11 M. Uehara, N. Gennai, M. Fujiwara and T. Tanaka, *IEEE Trans. Magn.*, 2005, **41**, 3838–3843.
12 N. M. Dempsey, F. M. A. Walther and D. Givord, *Appl. Phys. Lett.*, 2007, **70**, 092509.
13 N. M. Dempsey, T. G. Woodcock, H. Sepehri-Amin, Y. Zhang, H. Kennedy, D. Givord, K. Hono and O. Gutfleisch, *Acta Mater.*, 2013, **61**, 4920–4927.
14 Z. X. Ye, X. T. Zhao, W. Liu, L. Liu, J. X. Wu, Y. Li, J. Ma, H. Z. Ju, Y. H. Song and Z. D. Zhang, *Surf. Interfaces*, 2023, **37**, 02697.
15 Y. Zhang, D. Givord and N. M. Dempsey, *Acta Mater.*, 2012, **60**, 3783–3788.
16 E. F. Kneller and R. Hawig, *IEEE Trans. Magn.*, 1991, **27**, 3588–3600.
17 N. de Jonge, Y. Lamy, K. Schoots and T. H. Oosterkamp, *Nature*, 2002, **420**, 393–395.
18 W. Liu, Z. d. Zhang, J. p. Liu, L. j. Chen, L. l. He, Y. Liu, X. k. Sun and D. J. Sellmyer, *Adv. Mater.*, 2002, **14**, 1832–1834.
19 W. B. Cui, S. J. Zheng, W. Liu, X. L. Ma, F. Yang, Q. Yao, X. G. Zhao and Z. D. Zhang, *J. Appl. Phys.*, 2008, **104**, 053903.
20 W. B. Cui, W. Liu, J. Li, F. Yang, Q. Zhang, X. G. Liu and Z. D. Zhang, *J. Phys. D: Appl. Phys.*, 2008, **41**, 245007.

21 W. B. Cui, Y. K. Takahashi and K. Hono, *Adv. Mater.*, 2012, **24**, 6530–6535.
22 W. B. Cui, H. Sepehri-Amin, Y. K. Takahashi and K. Hono, *Acta Mater.*, 2015, **84**, 405–412.
23 C. H. Li, X. T. Zhao, L. Liu, W. Liu, Z. X. Ye, J. X. Wu, J. Ma and Z. D. Zhang, *J. Appl. Phys.*, 2024, **136**, 083901.
24 Z. M. Dai, W. Liu, X. T. Zhao, Z. Han, D. Kim, C. J. Choi and Z. D. Zhang, *J. Appl. Phys.*, 2016, **120**, 163906.
25 S. Yazdani, J. Phillips, A. Mosey, T. Bsaibes, R. Decca and R. Cheng, *Crystals*, 2024, **14**, 119.
26 C. H. Li, X. T. Zhao, L. Liu, W. Liu, Z. X. Ye, J. X. Wu, Y. Li, J. Ma, H. Z. Ju, Y. H. Song and Z. D. Zhang, *J. Alloys Compd.*, 2023, **960**, 170876.
27 W. Chen, J. M. Luo, Y. W. Guan, Y. L. Huang, M. Chen and Y. H. Hou, *J. Phys. D: Appl. Phys.*, 2018, **51**, 185001.
28 Q. Li, Z. Chen, H. Chong, H. Guo, Z. Huang, Q. Zhou and W. Cui, *Mater. Res. Lett.*, 2025, **13**, 820–828.
29 A. Durgun, D. Ohmer, M. Katter, A. Thul, S. Steentjes, H. S. Amin, O. Gutfleisch and I. Dirba, *Adv. Eng. Mater.*, 2025, e202501145.
30 L. Huang, J. M. Luo, C. Y. Wang, W. X. Chai, X. S. Zhang, Y. H. Hou, W. Li, X. Yu, C. C. Zhong, H. Y. Mao, L. Z. Zhao and Y. L. Huang, *Intermetallics*, 2024, **165**, 108158.
31 Z. Liu, J. He and R. V. Ramanujan, *Mater. Des.*, 2021, **209**, 110004.
32 W. J. Gong, X. Wang, W. Liu, S. Guo, Z. H. Wang, W. B. Cui, Y. L. Zhu, Y. Q. Zhang and Z. D. Zhang, *J. Appl. Phys.*, 2012, **111**, 07A729.
33 Y. Li, X. T. Zhao, W. Liu, J. Ma, L. Liu, Y. H. Song, W. Y. Deng, L. J. Qi, X. G. Zhao and Z. D. Zhang, *J. Appl. Phys.*, 2020, **128**, 043903.
34 Z. Ye, X. Zhao, L. Liu, W. Liu, J. Wang, J. Wu, Y. Li, J. Ma, H. Ju and Z. D. Zhang, *Nanoscale*, 2023, **15**, 18775–18784.
35 C. Rong, H. Zhang, R. Chen, S. He and B. Shen, *J. Magn. Magn. Mater.*, 2006, **302**, 126–136.
36 X. Tang, J. Li, H. Sepehri-Amin, A. Bolyachkin, A. Martin-Cid, S. Kobayashi, Y. Kotani, M. Suzuki and A. Terasawa, *NPG Asia Mater.*, 2023, **15**, 50.
37 T. G. Woodcock, Y. Zhang, G. Hrkac, G. Ciuta, N. M. Dempsey, T. Schrefl, O. Gutfleisch and D. Givord, *Scr. Mater.*, 2012, **67**, 536–541.
38 G. Hilscher, R. Grössinger, S. Heisz, H. Sassik and G. Wiesinger, *J. Magn. Magn. Mater.*, 1986, **54–57**, 577–578.
39 L. Zhao, J. Zhou, Q. Liu, Y. Yu, Z. Li, M. Li and P. Wang, *ACS Omega*, 2025, **10**, 48433–48443.
40 H. Rahimi, A. Ghasemi, R. Mozaffarinia and M. Tavoosi, *J. Magn. Magn. Mater.*, 2017, **429**, 182–191.
41 Z. Dai, K. Li, Z. Wang, W. Liu and Z. D. Zhang, *Materials*, 2022, **15**, 7648.
42 C. R. Pike, A. P. Roberts and K. L. Verosub, *J. Appl. Phys.*, 1999, **85**, 6660–6667.
43 C. R. Pike, *Phys. Rev. B:Condens. Matter Mater. Phys.*, 2003, **68**, 104424.
44 C. R. Pike, C. A. Ross, R. T. Scalettar and G. Zimanyi, *Phys. Rev. B:Condens. Matter Mater. Phys.*, 2005, **71**, 134407.
45 C. R. Pike, A. P. Roberts and K. L. Verosub, *Geophys. J. Int.*, 2001, **145**, 721–730.